frontiers | Frontiers in Physics

TYPE Original Research
PUBLISHED 12 February 2026
DOI 10.3389/fphy.2026.1698522

OPEN ACCESS

EDITED BY
Ioanna Kyriakou,
University of Ioannina, Greece

REVIEWED BY
Jake Harold Pensavalle,
Centro Pisano Multidisciplinare sulla Ricerca e Implementazione Clinica della Flash Radiotherapy (CPFR), Italy
Alexis Papadopoulos,
University of Ioannina, Greece

*CORRESPONDENCE
Yasmin Hamad,
yasmin.hamad@dkfz-heidelberg.de

RECEIVED 03 September 2025
REVISED 22 November 2025
ACCEPTED 09 January 2026
PUBLISHED 12 February 2026

CITATION
Hamad Y, Barna S, Magrin G, Palmans H, Sari FK, Gehrke T and Mairani A (2026) Radiation quality assessment in a clinical helium-ion beam using a SOI microdosimeter and a Timepix3 detector.
Front. Phys. 14:1698522.
doi: 10.3389/fphy.2026.1698522

Radiation quality assessment in a clinical helium-ion beam using a SOI microdosimeter and a Timepix3 detector

Yasmin Hamad[1,2,3,4]*, Sandra Barna[5,6], Giulio Magrin[5], Hugo Palmans[5,7], Ferisya Kusuma Sari[8], Tim Gehrke[1,8,9] and Andrea Mairani[1,2,4]

[1]Heidelberg Institute for Radiation Oncology (HIRO), National Center for Research in Radiation Oncology (NCRO), Heidelberg, Germany, [2]Clinical Cooperation Unit Translational Radiation Oncology, German Cancer Consortium (DKTK) Core-Center Heidelberg, National Center for Tumor Diseases (NCT), Heidelberg University Hospital (UKHD) and German Cancer Research Center (DKFZ), Heidelberg, Germany, [3]Faculty of Physics and Astronomy, Heidelberg University, Heidelberg, Germany, [4]Heidelberg Ion-Beam Therapy Center (HIT), Department of Radiation Oncology, Heidelberg University Hospital, Heidelberg, Germany, [5]MedAustron Ion Therapy Centre, Wiener Neustadt, Austria, [6]Medical University of Vienna, Vienna, Austria, [7]National Physical Laboratory, Teddington, United Kingdom, [8]Department of Medical Physics in Radiation Oncology, German Cancer Research Center (DKFZ), Heidelberg, Germany, [9]Department of Radiation Oncology, Heidelberg University Hospital, Heidelberg, Germany

Accurate characterization of radiation quality is essential for assessing radiobiological effects in radiotherapy, yet remains a major challenge. As modern treatment strategies increasingly consider not only absorbed dose but also linear energy transfer (LET) as a radiation quality specifier, the need for reliable tools to measure radiation quality in clinical settings is growing. While physical dose is routinely measured during quality assurance procedures, the experimental assessment of radiation quality is still limited. Microdosimetry offers a promising approach to address this gap. In this study, radiation quality is assessed through a microdosimetric approach using two advanced active solid-state detectors with distinct geometries: a 3D-mushroom Silicon-On-Insulator (SOI) microdosimeter developed at the University of Wollongong and a hybrid silicon-pixel Timepix3 detector. Although both being silicon-based, their differing geometries, sensor thicknesses, and detection principles lead to notable variations in their energy deposition spectra. The response functions of the two detection systems exposed to an initially monoenergetic 149.02 MeV/u helium pristine peak are compared in terms of spectral distributions and their expectation values. Experimental data are complemented with Monte Carlo simulations performed using the FLUKA code to validate and interpret the measurements. The advantages and limitations of both detection systems are discussed in the context of efforts to standardize radiation quality measurements. Such standardization could facilitate the integration of LET-based dosimetry into treatment planning systems, thereby improving the precision of radiobiological damage assessments. Ultimately, accounting for detector-specific response differences is crucial for establishing protocols for experimental verification of radiation quality in radiotherapy, as no standard

device or accredited experimental methodology has been unequivocally identified yet.

KEYWORDS

helium-beam radiotherapy, microdosimetry, linear energy transfer, silicon pixel Timepix3 detector, silicon on insulator, particle therapy

1 Introduction

Particle therapy continues to advance in cancer treatment, with protons and carbon ions as the leading therapies [1]. More recently, helium-ion therapy has emerged as a promising intermediate option with physical and radiobiological properties between the two [2]. However, its clinical implementation is still in its early stages and further research is needed to support its clinical spread [3, 4].

A key challenge in particle therapy is accurately linking physical radiation parameters to biological outcomes. The biological effects of an ionizing radiation depend on several factors, including the amount of radiation delivered (dose, fluence), the temporal pattern of delivery (dose rate, fractionation), and the spatial pattern of energy deposition (track structure). Among these, radiation quality, which is determined by the types and energies of charged particles at the site of interest, is pivotal for understanding and probing the underlying mechanism of radiobiological effects.

The pioneering experiments by Zirkle [5], along with many subsequent studies [6–8], have established that radiation-induced biological damage depends not only on the absorbed dose but also on the spatial distribution and track structure of the energy deposition at the microscopic level.

To quantify the heterogeneity of energy deposition in and near the tracks of charged particles, the linear energy transfer (LET) was introduced as a radiation quality specifier. LET is defined as the average energy deposited per unit length along a particle track, serving as a measure of ionization density. However, Let alone does not fully capture the stochastic nature of energy deposition events. It has been widely reported [9–11] that dose-averaged LET (LET_d) serves only as a coarse predictor of biological effects. Notably, similar LET_d values can arise from distinctly different underlying radiation field compositions, which can result in divergent cell survival outcomes and variations in relative biological effectiveness (RBE).

To address these limitations, microdosimetry has emerged as a refined framework for assessing radiation quality, enabling a more accurate characterization of the energy imparted at the cellular level. A major challenge in defining a consistent radiation quality specifier lies in the lack of a clear consensus on the material and dimensions of the critical volume representing the biological target. Over the past few decades, various radiobiological models have attempted to elucidate and predict radiation-induced biological effects across different damage scales, using biological target representations spanning nanometer [12, 13], micrometer [14, 15] and millimeter [16] scales, or multiple scales together [17–20].

Building on this, an additional challenge arises when detectors with differing geometries and volumes record significantly different energy deposition spectra for the same radiation field. This raises the question of how such differences in detector response should be interpreted in the context of radiation quality assessment and most importantly biological effect prediction. Furthermore, correlating spectra from different detector systems is essential to ensure consistent quality assurance (QA) and to strengthen their applicability in radiobiological modeling.

This study aims to investigate how radiation quality can be measured experimentally and which detection systems are well-suited for this purpose.

Despite gas-filled mini-tissue equivalent proportional counters remaining widely used in microdosimetry [21, 22], their high voltage operation (600–800 V) and fluence rate limitations (≤92 kcps) would make them less practical for QA workflows. Furthermore, passive detectors such as optically stimulated luminescence detectors (OSLDs), fluorescent nuclear track detectors (FNTDs), and thermoluminescent dosimeters (TLDs) are commonly used for radiation quality measurements. However, they lack real-time capabilities and typically require time-consuming post-irradiation readouts [23–25]. Moreover, since TLDs and OSLDs provide a signal integrated over the detection volume, spectral information cannot be retrieved. In this context, active detectors are a *sine qua non* for future routine clinical applications due to their ability to perform online measurements.

Specifically, we employed two active solid-state detection systems–a hybrid silicon pixel detector based on Timepix3 detector technology and a silicon-on-insulator (SOI) microdosimeter–which share silicon as the sensitive material but differ in geometry and dimensions. Although both are commonly used in research, standardized protocols for radiation quality measurement are still lacking. We assess their respective strengths, limitations and feasibility for clinical QA routines, focusing on key parameters including operation at clinical beam intensities, compatibility with different particle types, user-friendly setup, and standalone data post-processing. These measurements, while not directly used for RBE modelling in the present study, could provide valuable insights for improving RBE predictions [26, 27] and contribute to the broader effort of characterizing radiation quality in helium-ion therapy. While not yet standard clinical practice, LET-optimized treatment plans [3] have shown potential for improved treatment outcomes, reinforcing the need for accurate, spatially resolved measurements of radiation quality. Currently, helium ion TPS rely exclusively on a Monte Carlo (MC) derived database to compute LET distributions, but these values remain unvalidated experimentally.

2 Materials and methods

2.1 Microdosimetry formalism

In microdosimetry, radiation quality is quantitatively described by the lineal energy, y, defined as the ratio of the energy imparted by a single-event energy deposition, ϵ, to the mean chord length, $\bar{l}$, of a given volume. For the highly directional helium beam crossing

a non-isotropic slab volume considered in this work, lineal energy is defined following the ICRU report on Microdosimetry [28] as the energy imparted divided by the detector thickness [29]. The lineal energy is a stochastic quantity and it is useful to consider its cumulative distribution function *F(y)*, which represents the probability that the lineal energy is equal to or less than *y*. The corresponding lineal energy probability density function, *f(y)*, is the derivative of *F(y)* with respect to *y*:

$$f(y) = \frac{dF(y)}{dy}$$

It is important to note that *y* is defined for single energy-deposition events and it is independent of absorbed dose or dose rate. Expectation values of the *f(y)* distribution are the frequency-mean and dose-mean lineal energies:

$$\bar{y}_F = \int_0^\infty y f(y) dy;$$
$$\bar{y}_D = 1/\bar{y}_F \int_0^\infty y^2 f(y) dy = \int_0^\infty y d(y) dy \quad (1)$$

where *d(y)* is the dose probability density of *y*.

However, experimental measurements are limited by a threshold at low lineal energy due to electromagnetic noise, and by a high lineal energy cutoff, caused by saturation of the amplification gain. Consequently, the definition of $\bar{y}_F$ and $\bar{y}_D$ as defined in Equation 1, cannot be strictly met by a measurement, thus truncated forms of these quantities are introduced [30]. These are denoted as $\bar{y}_F^t$ and $\bar{y}_D^t$ and are defined as:

$$\bar{y}_F^t = \int_{y_{low}}^{y_{high}} y f(y) dy;$$
$$\bar{y}_D^t = 1/\bar{y}_F^t \int_{y_{low}}^{y_{high}} y^2 f(y) dy = \int_{y_{low}}^{y_{high}} y d(y) dy \quad (2)$$

where y_{low} and y_{high} represent, respectively, the lower lineal energy threshold imposed by the specific measurement (i.e., influenced by electromagnetic noise) and upper lineal energy limit determined by the detector's dynamic range.

The definition of the lineal energy is retained when describing the energy imparted per unit length per single event scored in the Timepix3 detector. Although the sensitive volume of the Timepix3 detector (thickness ~300 μm) is substantially larger than that of conventional microdosimeters (~1–10 μm), the ICRU Report 85 [31] definition of lineal energy remains applicable. In this work, the quantities measured by both detectors are therefore referred to as lineal energy, while explicitly acknowledging that the sensitive volumes differ in thickness by more than an order of magnitude.

2.2 Detection systems

Two active silicon-based detectors were employed: a hybrid silicon-pixel Timepix3 detector and a SOI microdosimeter. These systems, while sharing a common sensitive material, differ significantly in architecture, readout, fluence-rate limits, thresholds of imparted-energy spectra, and data handling approaches. Their distinct architecture and data handling are described in the following sections.

2.2.1 SOI microdosimeter

2.2.1.1 Device architecture

A "3D mushroom" silicon microdosimeter, developed at the Center for Medical Radiation Physics of the University of Wollongong (Australia), was used in this study. The device consists of a single sensitive volume (SV) having a diameter of 30 μm and a thickness of 10 μm. It is fabricated on a high resistivity p-type silicon on insulator (p-SOI) wafer using 3-dimensional detector technology [32] and it is attached to a low resistivity supporting wafer with a 2 μm silicon oxide between these two layers. Details on the device fabrication and technology can be found in Tran et al. as in Ref. [33]. Figure 1A presents a schematic and an image of the microdosimeter structure.

The microdosimeter measures current pulses proportional to the energy deposited by a single event. These signals are integrated into voltage pulses via a charge-sensitive electronic chain, consisting of an A250CF CoolFET charge-sensitive preamplifier and an ORTEC 671 low noise spectroscopy-based shaping amplifier. The pulse height spectra (PHS) were recorded using an ORTEC 928 MCB multi-channel analyzer (MCA) connected to a PC for data acquisition via the MAESTRO software. The schematic representation of the experimental set-up is shown in Figure 1B.

2.2.1.2 Linearization and calibration

The PHS obtained require calibration to retrieve the original deposited energy information. Firstly, the data collected were linearized to account for the nonlinear response in the amplification chain. This is achieved by establishing a correlation between the charge injected using a voltage pulse generator (mV) into the test capacitance of the preamplifier and the channel number in the PHS. The linearization was performed following the double-linearization method proposed by Meouchi [34] based on the piecewise function:

$$h_{lin} = \begin{cases} N \cdot a_1 + b_1, & 0 \le N < N_t \\ N \cdot a_2 + b_1 + (a_1 - a_2) \cdot N_t, & N > N_t \end{cases} \quad (3)$$

where h_{lin} is the linearized signal amplitude, N is the signal amplitude in the acquisition-channels units and a_1, a_2 and b_1 are fit parameters, and N_t is a free parameter optimized to minimize the sum of the squares of the residuals when fitting the linearization data obtained by employing a pulse generator.

The calibration in lineal energy was performed according to the particle edge method [35, 36]. This method involves identifying the "edge" of the spectrum, which corresponds to the maximum energy that an incident primary particle can deposit in the detector's SV. The edge is determined by fitting the upper region of the spectrum with a Fermi-like function and finding the intercept of the tangent through the inflection point with the horizontal axis as shown in Figure 2. For helium ions, the tangent to the sigmoid crosses the horizontal axis at a pulse value of 498.21 mV. This value was then assigned to the maximum lineal energy that a helium ion may impart to the SV of the detector. The maximum energy lost by the particles traversing the SV was calculated as the maximum energy

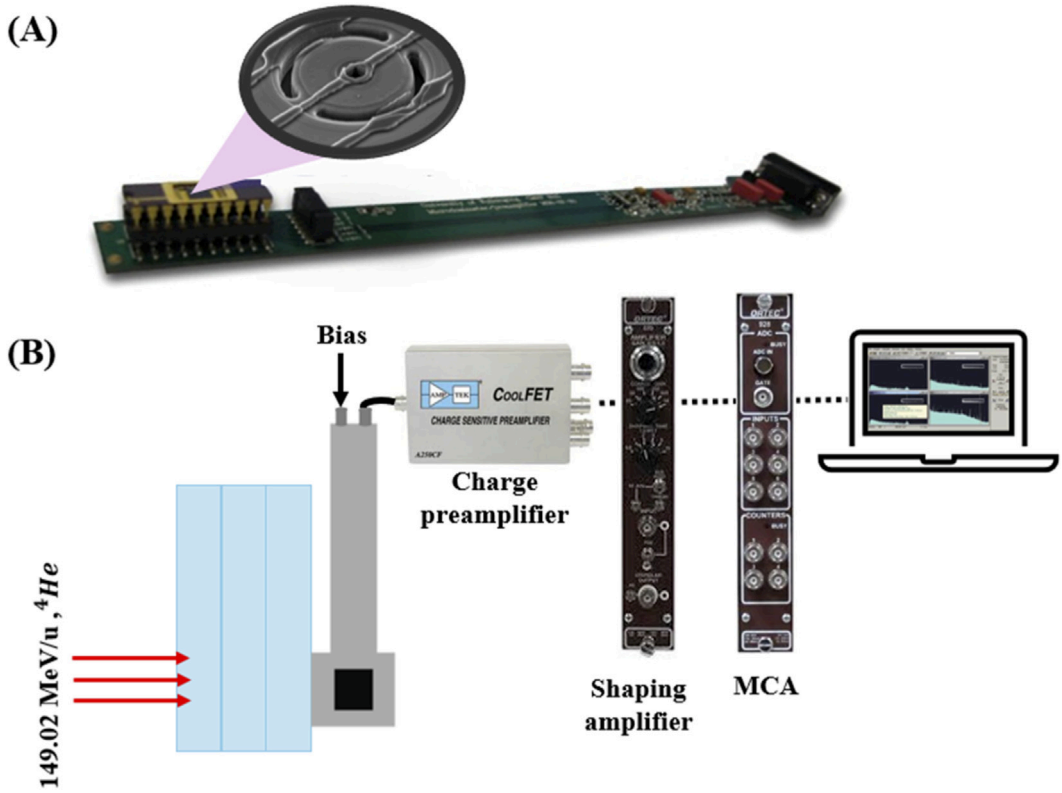

FIGURE 1
(A) Photo of the SOI microdosimeter and SEM image of the tranched-3D design of a single 3D Mushroom microdosimeter sensitive volume. **(B)** Schematic set-up for the experimental measurements.

for which the residual-range difference in the continuous slowing down approximation (CSDA) matches the thickness of the SV of the microdosimeter [34]. The stopping power tables for helium ions in silicon were retrieved from ICRU Report 49 lookup tables [37]. Under this assumption, the helium-edge corresponds to a lineal energy of 264.59 keV μm^{-1} in silicon. The calibrated data in silicon were then binned logarithmically and expectation values were calculated following the microdosimetry formalism.

2.2.2 Timepix3 detector

The Timepix3 hybrid pixel detector, developed at CERN within the Medipix3 collaboration [38, 39], features a 256 × 256 pixel matrix (65 536 pixels) with a 55 µm pitch, covering a sensitive area of 1.98 cm^2. A silicon sensor is bump-bonded to a highly integrated Application Specific Integrated Circuit (ASIC), where each pixel contains a charge-sensitive amplifier, threshold discriminator, 14-bit counter, and Wilkinson-type analog-to-digital converter (ADC). This architecture provides a high-granularity matrix of closely packed pixels, each with fully independent signal readout electronics (see Figure 3). The detector supports a 48-bit-data driven readout per pixel in the simultaneous time-of-arrival (ToA) and time-over-threshold (ToT) acquisition. In this mode, a continuous stream of data including pixel coordinates, ToA and ToT is generated.

The per-pixel information enables measurements of the deposited energy via ToT and the arrival time of single ions, which form clusters of hit pixels as they pass through the detector. To compensate for pixel-to-pixel threshold fluctuations related to variations in electronic components and ensure noise-free data acquisition, a 3 keV energy threshold for each pixel was individually adjusted using a 4-bit digital-to-analog converter. This procedure, known as threshold equalization, is described in Poikela et al. [38].

In this study, we used the AdvaPIX Timepix3 detector equipped with a 300 µm silicon sensor [40]. The compact device (125 × 79 × 25.5 mm^3, 503 g) connects via USB 3.0 for power, control, and readout. Data acquisition and visualization were performed using the PIXET Pro software.

2.2.2.1 Data post-processing

When a particle interacts with the silicon sensor, neighboring pixels around the interaction point can exhibit non-zero signals. This group of adjacent fired pixels with a ToT above threshold is referred to as a cluster. Clusters are formed due to diffusion and electric repulsion of electron-hole pairs created along the particle's path, which leads to a spread in charge collection across several neighboring pixels [41]. These processes occur during the signal collection and registration stages [42]. Each cluster of neighboring non-zero signals corresponds to an ionizing particle. The energy deposition information is inferred from the cluster volume, calculated as the sum of the individual keV values within a single cluster [43]. To convert ToT values into energy deposition, a per-pixel calibration was performed beforehand following a protocol based on X-ray fluorescence, as detailed in [44].

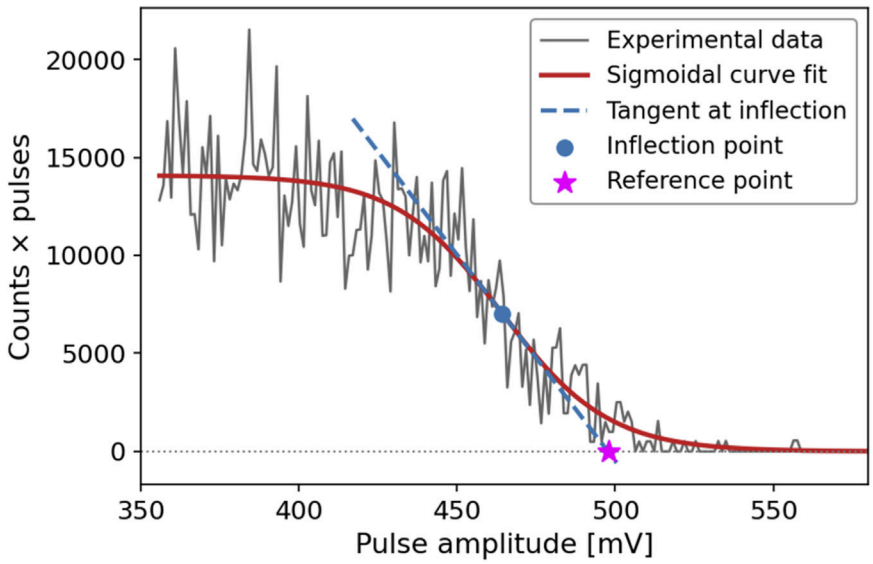

FIGURE 2
Edge calibration for the SOI-microdosimeter exposed to a 149.02 MeV/u helium-ion beam. The spectra exhibiting the edge have been consolidated and linearized. The experimental data (gray) are fitted with a sigmoidal curve (red line). The tangent to the sigmoid (blue dashed line) intersects the horizontal axis at the pulse value of 498.21 mV which corresponds to a lineal energy of 264.59 keV/μm in silicon.

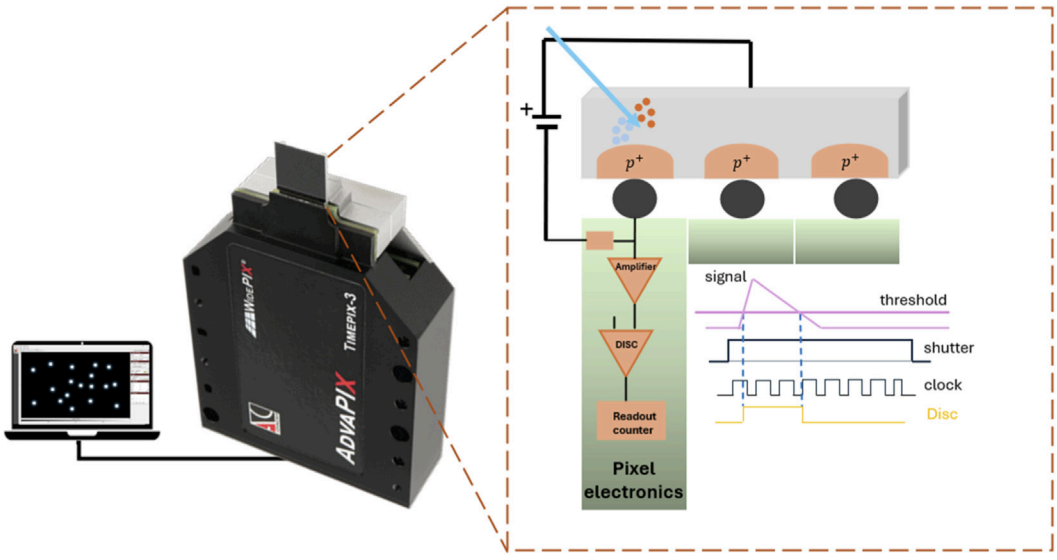

FIGURE 3
Picture and schematic of the operational setup for the Timepix3 detector with an inset of the sensitive silicon-layer bump-bonded to the electronic readout (not to scale). The gray layer indicates the silicon sensor layer, including the high-resistivity n-type and p-type regions. A blue arrow emulates the trajectory of an incoming charged particle. Electrons and holes are represented by light blue and orange dots within the silicon sensor. The diagram also shows the bump bonds, the pixelated readout layer, and the Timepix3 electronics chip and operation in ToT mode.

The algorithm for identifying clusters of adjacent non-zero signals from the measurement raw data is detailed elsewhere [45, 46]. A maximum time difference between neighboring pixels was set to 850 ns. Clusters detected near the sensor edge (i.e., the six outermost pixel columns and rows) were excluded from the data analysis to avoid spatial truncation. Additionally, cropped clusters due to erroneous time stamps assignments were identified and corrected in the same algorithm [40, 47]. Subsequently, energy deposition distributions were recalibrated to address saturation effects mainly caused by the so-called volcano-effect. The recalibration based on a saturating exponential fit followed the relationship:

$$\left\langle E_{dep}^{rec} \right\rangle_i = \frac{-1}{k} ln \frac{p - \left\langle E_{dep} \right\rangle_i}{q} \quad (4)$$

with k = 0.16 ± 0.01, p = 6.39 ± 0.25, q = 6.40 ± 0.25. Further details about the data post-processing can be found in [40].

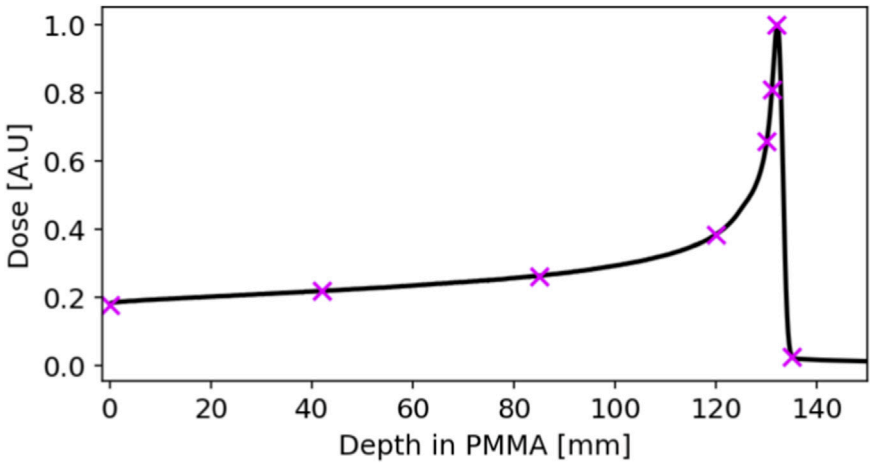

FIGURE 4
MC simulated depth-dose profile of the 149.02 MeV/u helium-ion beam employed for the experiment. The markers show the measurement points. The Bragg curve is scored without ripple filter in the beam path.

The recalibrated energy deposition spectra were then linearly rescaled by a constant track-length, corresponding to the partially depleted detector thickness. Expectation values of spectra in lineal energy were calculated following the microdosimetry formalism.

2.3 Irradiation setup

Irradiations were conducted in the experimental room of the Heidelberg Ion-Beam Therapy center (HIT) in Germany [48]. Both detectors were individually aligned to the isocenter using crosshair lasers, and measurements were performed downstream of polymethyl methacrylate (PMMA) slabs with perpendicular irradiation to the detector surface. The Timepix3 detector was operated in a partially depleted mode with 10 V bias voltage, corresponding to a 137 μm ± 3 μm [49] partially depleted thickness, while the SOI microdosimeter was operated at a bias voltage of 12 V.

Measurements were performed along the beam axis for a single-spot 149.02 MeV/u helium-ion pencil beam, both free in air and at PMMA depths of 42 mm, 85 mm, 120 mm, 130 mm, 131 mm, 132 mm, and 135 mm (see Figure 4). These PMMA depths refer to the actual geometrical thicknesses of the slabs and do not account for differences in the water equivalent thickness (WET) introduced by the detector housings. The corresponding $R_{90,distal}$ in PMMA of the Bragg curve was 133 mm and the full width at half maximum (FWHM) of the spot in air, upstream the PMMA phantom, was 11.1 mm. To minimize pile-up effects within the Timepix3 detector and ensure accurate detection of individual ion events, the flux (beam current) was reduced by two to three orders of magnitude compared with respect to the lowest clinical intensity (i.e. 10^6–10^7 ions s^{-1}), achieving a rate of 10^4–10^5 ions s^{-1}. The relatively small sensitive area of the SOI detector allowed great performance at clinical fluence rates where the device could be operated at a particle rate of 10^8 ions s^{-1} without noticeable pile-up distortions.

Furthermore, an air cooling system was employed to stabilize the Timepix3 detector temperature at around 26 °C and prevent energy threshold drifts caused by thermal fluctuations [50]. For the SOI microdosimeter, based on the spectrum acquisition, two different amplification gains (10:1) were used to cover specific dynamic ranges. The medium gain was applied for spectra acquired near or beyond the Bragg peak, while the high gain was used for spectra in the plateau region. Switching between gain settings was necessary to address the saturation of the high-gain, which would otherwise lead to incomplete spectra and, in particular, the loss of the edge region. As a result, the effective dynamic range of the measurement changes with depth. This option was not available in the Timepix3 detector due to the absence of an adaptive gain in this particular detector generation.

2.4 Uncertainty budget

Uncertainties in the expectation values derived from the SOI microdosimeter measurements are associated with a relative 5% uncertainty contribution from the stopping power data at low helium energies [51]. This contribution, propagated through the edge calibration, is the dominant source of uncertainty in $\bar{y}_F^t$ and $\bar{y}_D^t$ [34, 52, 53]. Other sources–such as electronic response non-linearity, marker point assessment for edge calibration and detector thickness determination–were comparatively minor and were considered negligible.

For the Timepix3 detector, the uncertainty budget is primarily driven by uncertainties in the fit parameters used for the recalibration of the measured energy deposition (c.f. Equation 4). These uncertainties were propagated into the final expectation values. Three recalibration scenarios were considered—mean, upper and lower bounds—corresponding to shifts along the x-axis of the energy deposition spectra, which in turn affect the derived quantities. Moreover, applying a non-linear recalibration function–derived from mean energy depositions to single-ion energy depositions [40]–introduces an additional mathematical systematic uncertainty ranging from 0.2% to 17.1%, with an

TABLE 1 Summary of the main sources of uncertainty for the SOI microdosimeter and Timepix3 detector, showing the qualitative impact of each uncertainty on the measured spectra and their typical magnitude.

Detector	Source of uncertainty	Effect on spectra	Magnitude
SOI microdosimeter	Edge calibration	Shifts spectrum along x-axis	~5% (associated with stopping power lookup tables)
	Linearization	>Shifts spectrum along x-axis and introduces spectral distortions	Negligible
Timepix3	Fit parameter of recalibration function	Shifts spectrum along x-axis and introduces spectral distortions	0.2%–17.1%, avg. 3.8%
	Temperature	Spectrum shifts toward lower energy with increasing temperature	Negligible due to air cooling system
Both	Counting statistics	Fluctuations in the spectra and impacts expectation values computation [54]	Negligible (>1 million events)

average of 3.8%. This was treated as an independent contribution, combined in quadrature with the fit parameter uncertainty. Overall, the combined average uncertainty across all measurements was approximately 8.4%.

Temperature-induced shifts of energy deposition were considered negligible, as the detector was maintained at a constant temperature using an air cooling system.

The only statistical uncertainty is the counting statistics that follows Poisson statistics. Since a large amount of events were collected for each position, typically exceeding 1 million, the statistical uncertainty of the spectra was found to be negligible compared to the systematic contributions. All uncertainties reported are expressed as standard uncertainties (coverage factor k = 1). A summary of the main sources of uncertainty and their impact on the measured spectra is presented in Table 1.

2.5 Monte Carlo simulations

MC simulations were conducted using the fully integrated particle physics simulation package FLUKA (version 2021.2) [55, 56]. The predefined physics settings for precision calculations were used by means of the PRECISIOn option in the DEFAULTS command. The COALESCE card was used to take into account the coalescence mechanism, a process in which high-energy light fragments can be produced by a mechanism that brings together nucleons that are proximate in phase space. The evaporation of heavy fragments was considered by activation of the EVAPORATION card. The simulation of those processes is required to achieve accurate results on the fragments production.

To account for the limited SV of the SOI microdosimeter, the thresholds for delta-ray production and transport were lowered relative to the default settings. Specifically, the delta-ray production threshold in silicon was set equal to the minimum allowed value of 1 keV. The particle step size within the SOI SV was constrained to 100 nm.

For simulations involving the Timepix3 detector, a higher delta-ray threshold of 100 keV was used due to its larger pixel pitch dimensions. Given that a 100 keV electron in silicon has a range in the CSDA of ~78 µm and considering the exclusion of outermost pixels during data post-processing (see Section 2.2.2), this threshold represents a good trade-off between accuracy and runtime performance.

A detailed model of the Timepix3 detector was implemented, encompassing all pertinent components essential for energy deposition scoring, without accounting for electronics-related effects. Conversely, the SOI microdosimeter SV was defined as a cylinder with a diameter and thickness of 30 µm and 10 µm, respectively. Any tape, plastic or aluminium housing surrounding the SV was omitted in the simulation. The simplified geometry has been shown to yield satisfactory agreement with experimental data, as reported by Barna et al. [57].

Moreover, for an accurate description of the transport and interactions of the beam with the traversed materials, the full beamline geometry of HIT has been included [58].

The energy deposition spectra were scored using a customized version of the MGDRAW routine. Further details on the MC simulation settings, detector geometries, and scoring parameters can be found in Supplementary Table S1 in the Supplementary Material.

3 Results

The spectra acquired with the two detection systems at four representative positions: the entrance region, the rising part of the Bragg curve, and two locations around the Bragg peak are plotted in Figure 5 in the form of frequency (A) and dose distributions (B). The spectra are normalized with respect to the peak due to the significant differences in the representation based on the normalization with respect to the area.

All spectra display a pronounced primary peak that progressively shifts toward higher lineal energy values as the depth in PMMA increases.

Noticeable spectral differences between the two detection systems in terms of primary peak positions and FWHM of the distributions were observed. The SOI microdosimeter consistently exhibits broader peaks values compared to Timepix3, particularly in the entrance region. The variance in the energy deposition spectra is influenced by energy-loss straggling, which decreases with increasing particle path length l_p; in

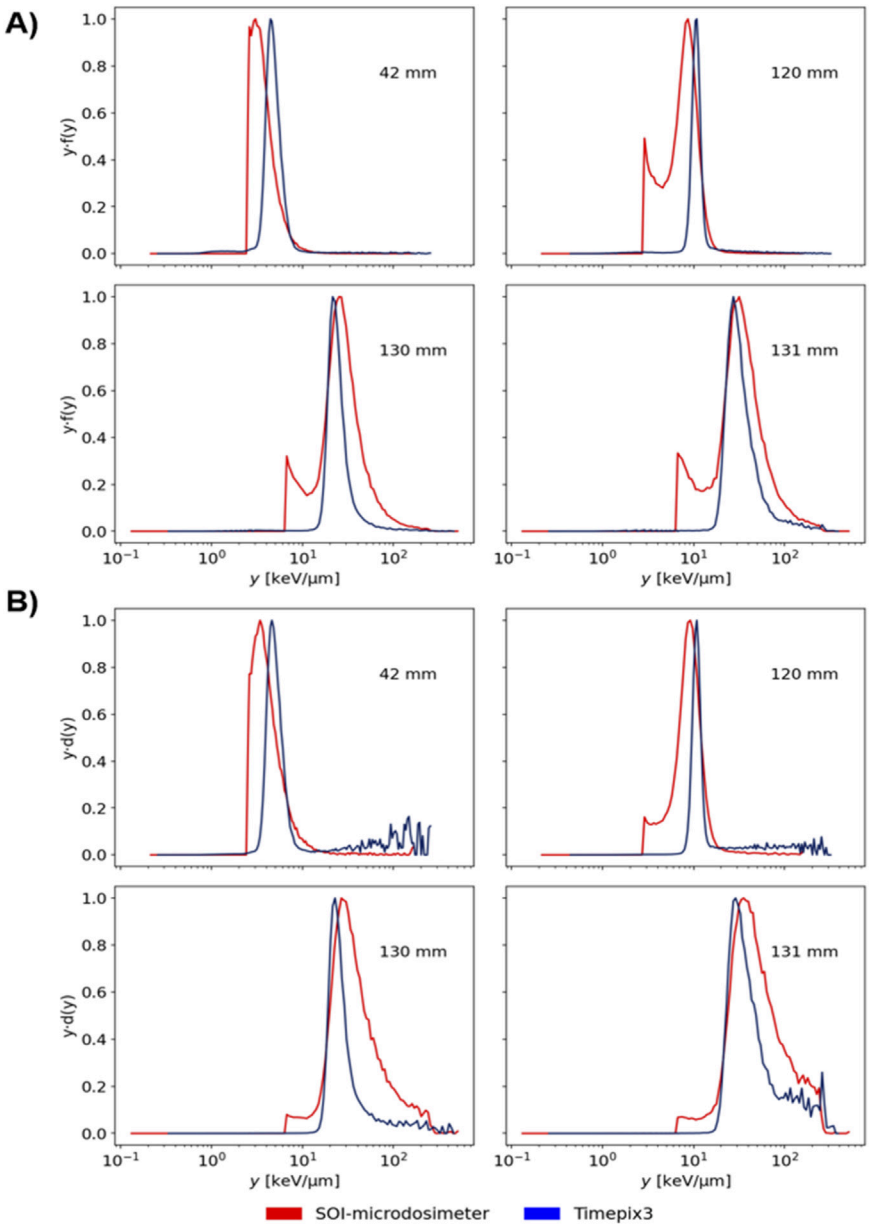

FIGURE 5
(A) Frequency, *yf(y)*, and **(B)** dose, *yd(y)*, distribution in lineal energy in the semi-log representation normalized with respect to the peak of a 149.02 MeV/u helium-ion beam measured by a SOI microdosimeter and a Timepix3 detector at different PMMA depths (42, 120, 130, and 131 mm). The spectra are reported without material conversion, i.e., silicon with density 2.33 g cm^{-3}.

this context, l_p corresponds to the SV thickness. A broader energy-loss spectrum is therefore expected for thinner detectors. This is due to the fact that the active SV of the Timepix3 is ~14 times thicker than the SOI and the number of primary collisions is higher. Under these conditions, the energy-loss straggling of the Timepix3 is smaller, in relative terms, than for the SOI.

As shown in Figure 5, the expected behavior was indeed observed where the spectra measured with the SOI microdosimeter are broader than those obtained with the Timepix3 detector. As an example, by fitting the frequency distribution *f(y)* with a Gaussian function at a depth of 120 mm in PMMA, the FWHM was 2.51 keV μm^{-1} and 5.42 keV μm^{-1} for the Timepix3 and SOI, respectively. However, the observed spectral broadening may also be influenced by experimental factors such as charge recombination or electromagnetic noise, which can further broaden the spectrum. The broader spectra observed in the SOI microdosimeter can also be attributed to chord-length variability, which is larger in cylindrical geometries compared to slab detectors [59].

In addition to differences in the FWHM (i.e., peak broadening), shifts in the primary peak position were observed. These discrepancies can be attributed to several factors, including differences in the WET of the detector housings (~0.3 mm), as well

as systematic uncertainties associated with the linearization (c.f. Equation 3) and calibration procedures of the SOI microdosimeter and the non-linear recalibration function applied to the Timepix3 measurements (c.f. Equation 4).

Specifically, uncertainties in the linearization and calibration procedures of the SOI microdosimeter can lead to a translation of the spectrum along the x-axis. On the other hand, the non-linear recalibration function introduces spectral distortions and shifts of the spectrum along the x-axis. Drifts in the peak positions of the *yd(y)* and *yf(y)* spectra can thus be attributed to drifts in the calibration procedures between the two detection systems. Despite the peak shifts, the peak in the *yd(y)* spectra corresponds approximately to the LET of the most probable particles at the specific depth.

As can be seen in Figure 6, the low lineal energy threshold for the SOI microdosimeter was generally too high to measure the whole contribution from lighter secondary fragments of higher energies (i.e., depositing very low lineal energy) due to the low signal-to-noise ratio. Since the low lineal energy threshold is an intrinsic limit of the experimental microdosimetry, different techniques have been proposed to extrapolate the missing part of the spectrum down to 0.01 keV/μm [60, 61]. Nevertheless, to be clinically relevant, the extrapolation method should reconstruct the fraction of dose associated with those events which could be estimated as the difference between the measured dose and the dose calculated from the microdosimetric measurement that considers only events above the detection threshold. Such extrapolation methods, however, are beyond the scope of this paper, as no extrapolation was applied to the presented data in order to focus solely on experimental observations. The detection threshold issue was particularly problematic when measuring the spectra in the entrance channel and in the distal tail, where only partial spectra were collected with the SOI. This may be associated with background electronic noise affecting either the detector or its electronic chain. As noted in Section 2.3, different amplification gains were applied, resulting in a cutoff in silicon ranging from approximately 3–5 keV/μm, depending on the shaping gain at the specific depth.

As primary helium ions approach the Bragg peak, their kinetic energy decreases significantly. A distinct helium-edge at higher lineal energies becomes evident in the spectra–particularly at depths of 130 mm and 131 mm in PMMA (c.f. Figures 5, 6). The edge corresponds to the maximum energy that can be deposited into a SV of a given thickness. This condition is reached when the ion's residual range is approximately equal to the detector's thickness, allowing the ion to stop within the SV. As a result, the position of the helium-edge varies with detector thickness. For the SOI microdosimeter, the helium edge corresponds to 264.59 keVμm^{-1}, while for the thicker Timepix3 detector, it shifts to 107.14 keVμm^{-1}. The trend is consistent with the findings of Parisi et al. [53], who reported that increasing detector thickness leads to a systematic shift of the particle-edge towards lower lineal energy values.

In the case of the SOI microdosimeter, this value was determined using a sigmoidal fit, as described in Section 2.2.1 and shown in Figure 2. In contrast, for the Timepix3 detector, the absence of a well-resolved edge in the measured spectra necessitated an estimation based on MC simulations. Previous studies, however, showed a distinct spectral ledge at higher lineal energies when the Timepix3 was exposed to a proton pristine peak [49]. By contrast, under helium irradiation, no clearly resolved edge is observed near 110 keVμm^{-1}. This lack of definition can be attributed to spectral distortions introduced by the non-linear recalibration function applied to correct signal saturation effects (i.e., the so-called volcano effect) [40].

Nonetheless, a drop in the *f(y)* distribution (Figure 6) at depth 130 mm in PMMA is still visible. However, this feature is not clearly resolved in the *yd(y)* spectra shown in Figure 5B, further indicating that spectral distortion may alter the true edge position.

The $\overline{y}_F^t$ and $\overline{y}_D^t$ values derived from the measured spectra are reported in Table 2. Although applying a higher common lineal energy cut-off could enhance the consistency of the intercomparison, in this study the unaltered experimental results were retained.

At the entrance channel, the $\overline{y}_F^t$ and $\overline{y}_D^t$ values obtained with the SOI microdosimeter are lower than those measured with the Timepix3 detector. However, this trend reverses in the region around the Bragg peak where the SOI yields higher values. The increase in $\overline{y}_D^t$ for the SOI in this region is intuitive, as the shift of the helium-edge towards higher lineal energy values leads to an increase in the dose-averaged lineal energy (c.f. Equation 2). Moreover, the fraction of primaries stopping within the SV increases moving along the Bragg curve. When a particle stops (i.e., stopper) in the SV, using the SV thickness as the mean path length overestimates the actual track length, making the measured lineal energy inaccurate. In regions with a higher fraction of stopping particles—whether primary ions or secondary fragments from the projectile or target—this effect introduces larger inaccuracies in the calculated expectation values. The fraction of stoppers depends on both the kinetic energy of the ion entering the SV and the SV thickness, becoming more significant at deeper positions along the Bragg curve and in thicker detectors. As a consequence, the contribution of the stoppers, and thus the underestimation of the resulting lineal energy, is more pronounced for the Timepix3 detector, leading to lower measured expectation values. When comparing the $\overline{y}_F^t$ one should consider the impact of the low lineal energy threshold that might affect the comparison. Since a relevant part of the microdosimetric spectrum is missing, the actual differences are expected to be higher than those observed.

Additionally, the role of secondary electrons (δ-rays) must be addressed, as their contribution affects the distinction between restricted and unrestricted radiation quality measurements. Monte Carlo simulations helped to investigate this as shown in Figure 7.

In slab detectors with large lateral dimensions–such as the Timepix3 detector (14 mm × 14 mm)–the variance introduced by δ-ray escape is expected to be negligible due to the high aspect ratio.

Conversely, detectors with a narrow transversal size under-represent the high-energy helium-ion losses and the peaks are moved toward lower lineal energies.

In the case of the SOI microdosimeter, δ-rays not associated with any primary ionizing event generate independent events that populate the lowest energy part of the spectrum. This increases the number of recorded events while decreasing the average energy deposited per event. This highlights the importance of considering δ-ray escape from detectors with limited lateral

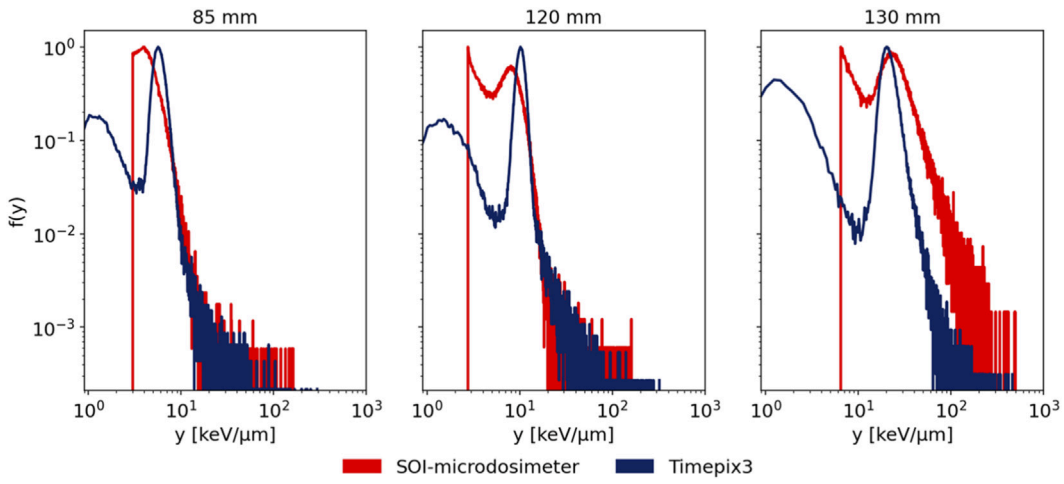

FIGURE 6
f(y) vs. *y* distribution in the log-log representation at different PMMA depths along the Bragg curve. The spectra are reported without material conversion i.e., silicon with density 2.33 g cm^{-3}.

TABLE 2 $\bar{y}_F^t$ and $\bar{y}_D^t$ of a 149.02 MeV/u helium-ion beam measured at different PMMA depths.

PMMA depth [mm]	$\bar{y}_F^t$ [keV/μm]		$\bar{y}_D^t$ [keV/μm]	
	SOI	Timepix3	SOI	Timepix3
0	3.2 ± 0.2	3.9 ± 0.4	4.8 ± 0.2	4.9 ± 0.3
42	3.9 ± 0.2	4.4 ± 0.4	5.3 ± 0.3	6.0 ± 0.6
85	5.0 ± 0.3	5.7 ± 0.5	6.6 ± 0.3	7.5 ± 0.8
120	7.8 ± 0.4	9.9 ± 0.9	10.2 ± 0.5	13.0 ± 1.1
130	30.6 ± 1.5	21.1 ± 2.1	48.6 ± 2.4	26.4 ± 2.1
131	38.2 ± 1.9	27.5 ± 2.7	62.1 ± 3.1	37.7 ± 3.6
132	46.1 ± 2.3	37.7 ± 3.2	76.7 ± 3.9	63.2 ± 5.5
135	5.1 ± 0.3	3.0 ± 0.3	15.1 ± 0.8	9.1 ± 0.1

Values are reported without material conversion. Uncertainties are reported with a coverage factor k = 1.

extensions (a few tens of micrometers), as it leads to a restricted measurement of radiation quality [62]. Notably, the δ-ray peak as the left peak in *yf(y)* in Figure 5A, contributes little to the dose distribution in lineal energy as observed in the *yd(y)* spectrum in Figure 5B but affects the radiation quality definition. In conclusion, Figure 7 highlights the importance of accurately characterizing secondary fragments and their contribution to the mixed radiation field [63]. Inelastic nuclear interactions of helium ions produce lighter secondary particles with sufficient kinetic energy and low lineal energy values, thereby dominating the left-hand tail of the distribution. Conversely, heavier target fragments, with higher energy deposition, populate the right-hand tail.

The comparison with experimental spectra demonstrates that the simulations reproduce both the overall shape and the primary peak corresponding to helium ions. The Timepix3 detector effectively resolves the contributions from projectile fragments in the left-hand tail, whereas the SOI microdosimeter, due to its relatively high low lineal energy threshold, does not resolve these events and exhibits a broader spectrum, consistent with previous studies [57, 64, 65]. On the right-hand side of the distribution, however, the SOI microdosimeter shows improved resolution for higher lineal energies compared to the shorter high-energy tail recorded with the Timepix3.

4 Discussion and conclusions

In this study, two active silicon-based detection systems—a hybrid pixel detector equipped with a Timepix3 chip technology

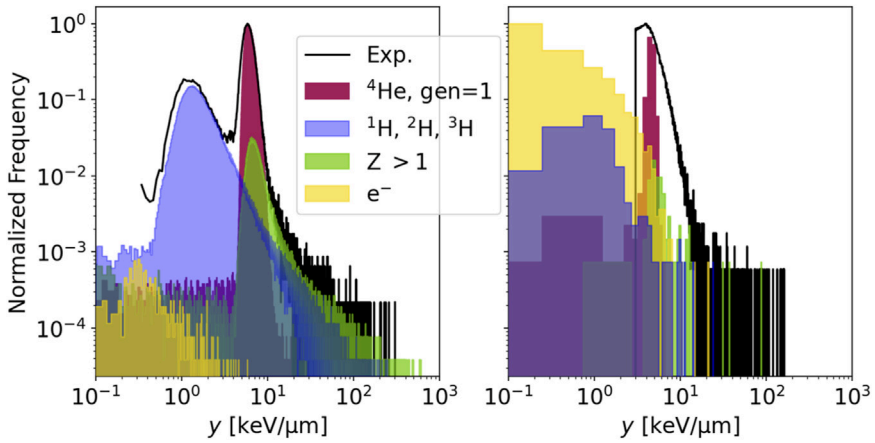

FIGURE 7
Simulated charged particle contributions within the sensitive volumes of the Timepix3 detector (left) and the SOI microdosimeter (right) after 85 mm of PMMA, compared to the corresponding experimental spectra. The simulated histograms show the distributions of primary helium ions, secondary light ions (protons, deuterons, and tritons), fragments with atomic number greater than 1 and secondary electrons that exceed the energy threshold and are not associated with any parent particle. Secondary electrons with energy above the production threshold are either attributed to the particle that produced them, and their energies are summed with that of the parent particle, or treated as independent events if no association with a particle crossing the detector volume is possible.

and a SOI microdosimeter—were compared for their suitability in characterizing radiation quality measurements in helium-ion therapy. The analysis focused on how differences in device architecture, SV size, volume, and geometry influence the measured energy deposition spectra. Both detectors enable rapid post-processing due to their active nature, making them promising candidates for integration into clinical quality assurance workflows. However, their respective architectures introduce distinct strengths and limitations. The Timepix3 detector offers unique capabilities for ion spectroscopy, enabling event-by-event discrimination between primary helium ions and secondary fragments [49, 66–68]. This feature is advantageous for TPS validation, where the computation of dose-averaged LET for helium-ion beams considers only particles with $Z \leq 2$. Including the contribution of secondary fragments can substantially affect the computed dose-averaged LET and the RBE [11].

Furthermore, its compact, user-friendly design with fully integrated readout electronics simplifies experimental handling and data acquisition. Nevertheless, Timepix3 operation requires a reduction of the fluence/dose rate below clinical settings. This can represent a downside in facilities where such settings are not feasible or allowed. Additionally, saturation effects and the absence of an adaptive gain, limit the per-pixel spectral range for carbon-ion measurements (c.f. Section 2.2.2).

While this represents a clear limitation for carbon-ion applications, similar effects were observed in the present measurements at the upper end of the recalibration dynamic range, where the saturating exponential recalibration function introduced distortions around the helium-edge region.

Its relatively large SV thickness also increases susceptibility to radiation damage due to the longer drift of charge carriers in the active region, which can degrade detector performance over time.

In contrast, the SOI microdosimeter demonstrates a better performance under clinical fluence rates due to its limited aspect ratio and has been validated as well for use with carbon ions [62, 69].

However, the low lineal energy threshold was a relevant issue impacting the accuracy of the microdosimetric spectra collected with the SOI microdosimeter especially in the entrance region.

In the present study, the lineal energy spectra exhibited a low lineal energy threshold of $y_{low} \sim 3$ keV/µm in silicon. For comparison, measurements performed in the HIT experimental room using a MicroPlus probe and diamond detector reported a threshold of $y_{low} \sim 1$ keV/µm in water. When applying a first-order constant material conversion from silicon to water [70, 71], these thresholds are comparable, highlighting that this low-energy threshold represents a common limitation across different experimental setups.

Additionally, due to its limited transversal size, the detector suffers more from δ-ray escape compared to the Timepix3, resulting in a restricted radiation quality measurement. This may hinder its application for TPS verification which relies on unrestricted LET values, namely, including the contribution of all secondary electrons.

While most recent studies using the Timepix3 report results of unrestricted LET measurements [47, 72], this classification should be interpreted with caution and requires further validation. Despite this, some publications have demonstrated the ability of the Timepix technology to detect δ-rays which manifest as thin, curly tracks emerging from the central ionization cluster [73].

To provide a concise overview of the distinct strengths and limitations of both detection systems, a summary of their advantages and disadvantages is presented in Table 3.

The choice of a radiation quality descriptor depends on the specific biological effect it is intended to predict. There is no golden standard descriptor; the optimal choice depends on the type of damage being investigated. Moreover, any radiation quality specifier

TABLE 3 Summary of the main advantages and disadvantages of the Timepix3 detector and SOI microdosimeter, highlighting differences in performance under clinical conditions, and suitability for radiation quality measurements in the context of QA applications.

Detector	Advantages	Disadvantages
Timepix3 detector	• Single-ion spectroscopy via event-by-event tracking • Compact, user-friendly design with integrated readout electronics • Enables rapid post-processing and straightforward integration into clinical QA workflows • High spatial resolution	• Operates at reduced fluences compared to clinical settings • Saturation effect hinders application with carbon-ions • Large SV thickness increases susceptibility to radiation damage. • Sensitive to thermal fluctuations; potential spectral drift without cooling system.
SOI microdosimeter	• Operates at clinical fluence rates without pile-up • Versatile across different particle types • Adjustable dynamic range for specific application • Established and recognized for potential QA applications.	• Low lineal energy threshold affected by electromagnetic noise • Delta-ray escape may underestimate unrestricted LET • Lacks ion spectroscopy capabilities • Cumbersome electronics and readout.

must be coupled with a model to translate physical measurements into predicted biological outcomes, making it challenging to disentangle the performance of the descriptor from that of the predictive model. Models differ not only in their assumptions but also in how they handle the radiation quality information, either by considering solely expectation values or the full energy spectrum [74, 75].

Spectral analysis (Figures 5, 6) revealed differences in peak broadness between the two detection systems, with implications for RBE estimation. As shown by Grün et al. [9], spectral energy variance significantly affects RBE prediction, reinforcing the importance of detector selection. It is important to emphasize that the observed spectral differences reflect differences in sensitive volume dimensions and measurement resolution, rather than differences in the underlying radiation quality. Both detectors sample the same radiation field, and with appropriately chosen radiobiological models, differing spectra may result in comparable RBE predictions—unless the detector misses details of the polyenergetic tracks in the energy deposition spectrum that are critical for the biological outcome. Therefore, the comparison does not imply that one detector is inherently superior; it highlights the need to account for geometrical and model-dependent effects when interpreting lineal energy spectra in relation to biological outcomes.

Domain size plays a crucial role in correlating measured spectra in lineal energy to RBE predictions, particularly when comparing detectors with fixed geometries. Noteworthy is the sensitivity of RBE predictions based on the modified microdosimetric kinetic model (mMKM) to microdosimetric function and domain geometry. This has an important implication for translating RBE estimates across different detector types and for clinical applications where target size and geometry must be accurately reflected. This reinforces the importance of understanding how modeling assumptions affect RBE predictions [76]. By setting *a priori* and keeping constant the mMKM parameters, spectra in lineal energy scored in different volumes would lead to significant differences in the predicted RBE. As a consequence, careful validation when implementing or modifying RBE models is needed. Spectral radiation quality measurements could offer valuable insight into this research quest when used in combination with radiobiological experiments.

In light of this study, the single-ion identification capabilities of the Timepix3 detector represent a significant advancement in high-resolution radiation quality monitoring. Its compact and user-friendly setup, combined with a straightforward data post processing, further facilitates its integration into clinical workflows. To enable its application at clinical beam intensities, future detector developments should explore hybrid pixel detectors equipped with newer readout chips, such as Timepix2 or Timepix4 [77–79]. Their adaptive gain extends the dynamic range and the improved digitalization of analog signals during the data readout facilitates an operation under clinical beam intensities. Additionally, a thinner silicon layer (~50 µm, based on current fabrication technologies) would mitigate saturation effects due to high energy deposition per pixel.

Moreover, to avoid shortcomings such as a dependence on thermal fluctuations in the SV or saturation effects in the electronics observed for hole collection, the hybrid architecture of the Timepix family of detectors could be employed in combination with a silicon carbide (SiC) or gallium arsenide (GaAs) sensor. SiC is a radiation-hard material and does not require a cooling system to stabilize the temperature [80]. However, the choice of the sensitive layer should be made with regard to tissue-equivalence conversion. A waterproof housing would also facilitate measurements with a motorized water phantom with a positioning resolution of approximately 100 µm. This is of extreme importance for radiation quality measurements performed in high-gradient regions of LET, where a small error in the detector position can result in significant energy spectra changes.

Such enhancements would preserve the advantages of the Timepix systems—including high spatial resolution, cluster-based ion identification, event-by-event analysis, and user-friendly operation—while extending its operational range.

The comparison of detection systems for radiation quality measurement addresses an underexplored need in clinical implementation of helium-ion therapy. The findings reported in this study highlight the importance of matching detector capabilities to specific clinical or research needs, particularly when validating TPS LET predictions or estimating RBE.

Data availability statement

The original contributions presented in the study are included in the article/Supplementary Material, further inquiries can be directed to the corresponding author.

Author contributions

YH: Conceptualization, Data curation, Formal Analysis, Investigation, Methodology, Software, Validation, Visualization, Writing – original draft, Writing – review and editing. SB: Conceptualization, Investigation, Resources, Validation, Writing – review and editing. GM: Conceptualization, Investigation, Resources, Supervision, Validation, Writing – review and editing. HP: Supervision, Validation, Writing – review and editing. FS: Investigation, Writing – review and editing. TG: Investigation, Resources, Supervision, Writing – review and editing. AM: Conceptualization, Funding acquisition, Methodology, Project administration, Resources, Supervision, Writing – review and editing.

Funding

The author(s) declared that financial support was received for this work and/or its publication. YH was funded by the Deutsche Krebshilfe (German Cancer Aid—Project No.: 70114371), and TG by the Deutsche Forschungsgemeinschaft (DFG, German Research Foundation—Project No.: 426970603).

Acknowledgements

The authors thank the HIT facility for providing the beam time for this work.

Conflict of interest

The author(s) declared that this work was conducted in the absence of any commercial or financial relationships that could be construed as a potential conflict of interest.

The reviewer AP declared a past co-authorship with the author(s) SB, GM, HP to the handling editor.

Generative AI statement

The author(s) declared that generative AI was not used in the creation of this manuscript.

Any alternative text (alt text) provided alongside figures in this article has been generated by Frontiers with the support of artificial intelligence and reasonable efforts have been made to ensure accuracy, including review by the authors wherever possible. If you identify any issues, please contact us.

Publisher's note

Supplementary material

The Supplementary Material for this article can be found online at: https://www.frontiersin.org/articles/10.3389/fphy.2026.1698522/full#supplementary-material

References

1. Tommasino F, Scifoni E, Durante M. New ions for therapy. *Int J Part Ther* (2015) 2:428–38. doi:10.14338/IJPT-15-00027.1

2. Mairani A, Mein S, Blakely E, Debus J, Durante M, Ferrari A, et al. Roadmap: helium ion therapy. *Phys Med Biol* (2022) 67(15). doi:10.1088/1361-6560/ac65d3

3. Tessonnier T, Mairani A, Chen W, Sala P, Cerutti F, Ferrari A, et al. Proton and helium ion radiotherapy for meningioma tumors: a Monte Carlo-based treatment planning comparison. *Radiat Oncol* (2018) 13(1):2. doi:10.1186/s13014-017-0944-3

4. Tessonnier T, Ecker S, Besuglow J, Naumann J, Mein S, Longarino FK, et al. Commissioning of helium ion therapy and the first patient treatment with active beam delivery. *Int J Radiat Oncol Biol Phys* (2023) 116(4):935–48. doi:10.1016/j.ijrobp.2023.01.015

5. Zirkle RE. Biological effectiveness of alpha particles as a function of ion concentration produced in their paths. *Am J Cancer* (1935) 23:558–67. doi:10.1158/ajc.1935.558

6. Paganetti H, Gerweck LE, Goitein M. The general relation between tissue response to x-radiation (alpha/beta-values) and the relative biological effectiveness (RBE) of protons: prediction by the Katz track-structure model. *Int J Radiat Biol* (2000) 76(7):985–98. doi:10.1080/09553000050051007

7. Scholz M, Kraft G. Track structure and the calculation of biological effects of heavy charged particles. *Adv Space Res* (1996) 18(1):5–14. doi:10.1016/0273-1177(95)00784-c

8. Rossi HH. Specification of radiation quality. *Radiat Res* (1959) 10(5):522–31. doi:10.2307/3570787

9. Grun R, Friedrich T, Traneus E, Scholz M. Is the dose-averaged LET a reliable predictor for the relative biological effectiveness? *Med Phys* (2019) 46(2):1064–74. doi:10.1002/mp.13347

10. Guan F, Bronk L, Kerr M, Li Y, Braby LA, Sobieski M, et al. Interpreting the biological effects of protons as a function of physical quantity: linear energy transfer or microdosimetric lineal energy spectrum? *Scientific Rep* (2024) 14(1):25181. doi:10.1038/s41598-024-73619-x

11. Parisi A, Furutani KM, Beltran CJ. Impact of nuclear fragmentation and irradiation scenarios on the dose-averaged LET, the RBE, and their relationship for H, He, C, O, and Ne ions. *Med Phys* (2025) 52(5):3450–60. doi:10.1002/mp.17755

12. Goodhead DT. Initial events in the cellular effects of ionizing radiations: clustered damage in DNA. *Int J Radiat Biol* (1994) 65(1):7–17. doi:10.1080/09553009414550021

13. Ottolenghi A, Merzagora M, Tallone L, Durante M, Paretzke HG, Wilson WE. The quality of DNA double-strand breaks: a Monte Carlo simulation of the end-structure of strand breaks produced by protons and alpha particles. *Radiat Environ Biophys* (1995) 34(4):239–44. doi:10.1007/BF01209749

14. Hawkins RB. A microdosimetric-kinetic model for the effect of non-poisson distribution of lethal lesions on the variation of RBE with LET. *Radiat Res* (2003) 160(1):61–9. doi:10.1667/rr3010

15. Hawkins RB. A statistical theory of cell killing by radiation of varying linear energy transfer. *Radiat Res* (1994) 140(3):366–74. doi:10.2307/3579114

16. McNamara AL, Schuemann J, Paganetti H. A phenomenological relative biological effectiveness (RBE) model for proton therapy based on all published *in vitro* cell survival data. *Phys Med Biol* (2015) 60(21):8399–416. doi:10.1088/0031-9155/60/21/8399

17. Friedrich T, Scholz U, Elsässer T, Durante M, Scholz M. Calculation of the biological effects of ion beams based on the microscopic spatial damage distribution pattern. *Int J Radiat Biol* (2012) 88(1-2):103–7. doi:10.3109/09553002.2011.611213

18. Grün R. Impact of enhancements in the local effect model (LEM) on the predicted RBE-weighted target dose distribution in carbon ion therapy. *Phys Med Biol* (2012) 57(22):7261–74. doi:10.1088/0031-9155/57/22/7261

19. Friedrich T, Ilicic K, Greubel C, Girst S, Reindl J, Sammer M, et al. DNA damage interactions on both nanometer and micrometer scale determine overall cellular damage. *Scientific Rep* (2018) 8(1):16063. doi:10.1038/s41598-018-34323-9

20. Palmans H, Rabus H, Belchior AL, Bug MU, Galer S, Giesen U, et al. Future development of biologically relevant dosimetry. *Br J Radiol* (2014) 88(1045):20140392. doi:10.1259/bjr.20140392

21. Conte V, Bianchi A, Selva A, Petringa G, Cirrone GAP, Parisi A, et al. Microdosimetry at the CATANA 62 MeV proton beam with a sealed miniaturized TEPC. *Phys Med* (2019) 64:114–22. doi:10.1016/j.ejmp.2019.06.011

22. Bianchi A, Selva A, Pasquato F, Rossignoli M, Minarello A, Fazzi A, et al. Microdosimetric measurements for LET monitoring in proton therapy. The development of engineered mini-TEPCs for clinical applications: first results. *Radiat Measurements* (2024) 177:107271. doi:10.1016/j.radmeas.2024.107271

23. Munoz ID. Linear energy transfer measurements and estimation of relative biological effectiveness in proton and helium ion beams using fluorescent nuclear track detectors. *Int J Radiat Oncol Biol Phys* (2024) 120(1):205–15. doi:10.1016/j.ijrobp.2024.02.047

24. Christensen JB, Muñoz ID, Bassler N, Stengl C, Bossin L, Togno M, et al. Optically stimulated luminescence detectors for dosimetry and LET measurements in light ion beams. *Phys Med Biol* (2023) 68(15). doi:10.1088/1361-6560/acdfb0

25. Yukihara EG, McKeever SWS, Andersen CE, Bos AJJ, Bailiff IK, Yoshimura EM, et al. Luminescence dosimetry. *Nat Rev Methods Primers* (2022) 2(1):26. doi:10.1038/s43586-022-00102-0

26. Mairani A, Magro G, Dokic I, Valle SM, Tessonnier T, Galm R, et al. Data-driven RBE parameterization for helium ion beams. *Phys Med Biol* (2016) 61(2):888–905. doi:10.1088/0031-9155/61/2/888

27. Mein S, Dokic I, Klein C, Tessonnier T, Böhlen TT, Magro G, et al. Biophysical modeling and experimental validation of relative biological effectiveness (RBE) for (4)He ion beam therapy. *Radiat Oncol* (2019) 14(1):123. doi:10.1186/s13014-019-1295-z

28. Braby LA, Conte V, Dingfelder M, Goodhead DT, Pinsky LS, Rosenfeld AB, et al. ICRU report 98, stochastic nature of radiation interactions: microdosimetry. *J ICRU* (2023) 23(1):1–168. doi:10.1177/14736691231211380

29. Bolst D, Guatelli S, Tran LT, Rosenfeld AB. Optimisation of the design of SOI microdosimeters for hadron therapy quality assurance. *Phys Med Biol* (2018) 63(21):215007. doi:10.1088/1361-6560/aae66b

30. Lennart Lindborg AW. *Microdosimetry: experimental methods and applications*. Boca Raton, FL: CRC Press/Taylor and Francis Group (2017).

31. Thomas DJ. *ICRU report 85: fundamental quantities and units for ionizing radiation*. Oxford University Press (2012).

32. Kok A. Fabrication and first characterization of silicon-based full 3-D microdosimeters. *IEEE Trans Nucl Sci* (2020). doi:10.1109/TNS.2020.3035077

33. Tran L. Thin silicon microdosimeter utilizing 3-D MEMS fabrication technology: charge collection study and its application in mixed radiation fields. *IEEE Trans Nucl Sci* (2017). doi:10.1109/TNS.2017.2768062

34. Meouchi C, Barna S, Puchalska M, Tran LT, Rosenfeld A, Verona C, et al. On the measurement uncertainty of microdosimetric quantities using diamond and silicon microdosimeters in carbon-ion beams. *Med Phys* (2022) 49(10):6699–715. doi:10.1002/mp.15929

35. Conte V. Lineal energy calibration of mini tissue-equivalent gas-proportional counters (TEPC). *AIP Conf Proc* (2013) 1530(1):171–8. doi:10.1063/1.4812920

36. Parisi A, Boogers E, Struelens L, Vanhavere F. Uncertainty budget assessment for the calibration of a silicon microdosimeter using the proton edge technique. *Nucl Instr Methods Phys Res Section A: Acc Spectrometers, Detectors Associated Equipment* (2020) 978:164449. doi:10.1016/j.nima.2020.164449

37. ICRU. Stopping powers and ranges for protons and alpha particles. In: *ICRU report 49, I.C.o.R.U.a. measurements* (1993).

38. Poikela T, Plosila J, Westerlund T, Campbell M, Gaspari MD, Llopart X, et al. Timepix3: a 65K channel hybrid pixel readout chip with simultaneous ToA/ToT and sparse readout. *J Instrumentation* (2014) 9:C05013. doi:10.1088/1748-0221/9/05/c05013

39. Ballabriga R, Campbell M, Llopart X. Asic developments for radiation imaging applications: the medipix and timepix family. *Nucl Instr Methods Phys Res Section A: Acc Spectrometers, Detectors Associated Equipment* (2018) 878:10–23. doi:10.1016/j.nima.2017.07.029

40. Felix-Bautista R. Towards precise LET measurements based on energy deposition of therapeutic ions in Timepix3 detectors. *Phys Med Biol* (2024) 69(12). doi:10.1088/1361-6560/ad5267

41. Jakubek J. Energy-sensitive X-ray radiography and charge sharing effect in pixelated detector. *Nucl Instr Methods Phys Res Section A: Acc Spectrometers, Detectors Associated Equipment* (2009) 607:192–5. doi:10.1016/j.nima.2009.03.148

42. Campbell M, Heijne E, Holý T, Idárraga J, Jakůbek J, Lebel C, et al. Study of the charge sharing in a silicon pixel detector by means of α-particles interacting with a Medipix2 device. *Nucl Instr Methods Phys Res Section A: Acc Spectrometers, Detectors Associated Equipment* (2008) 591(1):38–41. doi:10.1016/j.nima.2008.03.096

43. Granja C. Response of the pixel detector Timepix to heavy ions. *Nucl Instr and Methods Phys Res Section A-Accelerators Spectrometers Detectors Associated Equipment* (2011) A:633. doi:10.1016/j.nima.2010.06.166

44. Jakubek J. Precise energy calibration of pixel detector working in time-over-threshold mode. *Nucl Instr Methods Phys Res Section A: Acc Spectrometers, Detectors Associated Equipment* (2011) 633:S262–S266. doi:10.1016/j.nima.2010.06.183

45. Kelleter L, Schmidt S, Subramanian M, Marek L, Granja C, Jakubek J, et al. Characterisation of a customised 4-chip Timepix3 module for charged-particle tracking. *Radiat Measurements* (2024) 173:107086. doi:10.1016/j.radmeas.2024.107086

46. Schweins L. Detection of an internal density change in an anthropomorphic head phantom via tracking of charged nuclear fragments in carbon-ion radiotherapy. *Med Phys* (2024). doi:10.1002/mp.17590

47. Stasica-Dudek P, Granja C, Kopeć R, Krzempek D, Oancea C, Rucinski A, et al. Experimental validation of LET in intensity-modulated proton therapy with a miniaturized pixel detector. *Phys Med Biol* (2025) 70(9). doi:10.1088/1361-6560/adcaf9

48. Combs SE, Jäkel O, Haberer T, Debus J. Particle therapy at the Heidelberg Ion Therapy Center (HIT) - integrated research-driven university-hospital-based radiation oncology service in Heidelberg, Germany. *Radiother Oncol* (2010) 95(1):41–4. doi:10.1016/j.radonc.2010.02.016

49. Hamad Yasmin SFK, Renato F-B, Mária M, Andrea M, Tim G. LET measurements in proton and helium-ion beams of therapeutic energies using a silicon pixel detector towards a tool for quality assurance. *Med Phys* (2025). doi:10.1002/mp.18085

50. Urban M, Nentvich O, Marek L, Hudec R, Sieger L. Timepix3: temperature Influence on Radiation Energy Measurement with Si Sensor. *Sensors* (2023) 23:2201. doi:10.3390/s23042201

51. Ziegler JF, Ziegler MD, Biersack JP. SRIM–the stopping and range of ions in matter. *Nucl Instr Methods Phys Res Section B: Beam Interactions Mater Atoms* (2010) 268(11-12):1818–23. doi:10.1016/j.nimb.2010.02.091

52. Colautti DMP. Statistical and overall uncertainties in proton therapy microdosimetric measurements. (2010).

53. Parisi G, Magrin G, Verona C, Verona-Rinati G, Barna S, Meouchi C, et al. On the microdosimetric characterisation of the radiation quality of a carbon-ion beam and the effect of the target volume thickness. *Phys Med Biol* (2024) 69(24). doi:10.1088/1361-6560/ad965e

54. Parisi G, Schettino G, Romano F. A systematic study of the contribution of counting statistics to the final lineal energy uncertainty in microdosimetry. *Phys Med Biol* (2022) 67(15). doi:10.1088/1361-6560/ac79fb

55. Battistoni G, Bauer J, Boehlen TT, Cerutti F, Chin MPW, Dos Santos Augusto R, et al. The FLUKA code: an accurate simulation tool for particle therapy. *Front Oncol* (2016) 6:116. doi:10.3389/fonc.2016.00116

56. Collaboration TF, Ballarini F, Batkov K, Battistoni G, Bisogni MG, Böhlen TT, et al. The FLUKA code: overview and new developments. *EPJ Nucl Sci. Technol.* (2024) 10:16. doi:10.1051/epjn/2024015

57. Barna S. Microdosimetry of a clinical carbon-ion pencil beam at MedAustron, Part 2: Monte Carlo simulation. *Z für Medizinische Physik* (2025). doi:10.1016/j.zemedi.2025.04.005

58. Parodi K, Mairani A, Sommerer F. Monte Carlo-based parametrization of the lateral dose spread for clinical treatment planning of scanned proton and carbon ion beams. *J Radiat Res* (2013) 54(Suppl. 1):i91–6. doi:10.1093/jrr/rrt051

59. Conte V, Agosteo S, Bianchi A, Bolst D, Bortot D, Catalano R, et al. Microdosimetry of a therapeutic proton beam with a mini-TEPC and a MicroPlus-Bridge detector for RBE assessment. *Phys Med Biol* (2020) 65(24):245018. doi:10.1088/1361-6560/abc368

60. Bianchi A, Selva A, Colautti P, Parisi A, Vanhavere F, Reniers B, et al. The effect of different lower detection thresholds in microdosimetric spectra and their mean values. *Radiat Measurements* (2021) 146:106626. doi:10.1016/j.radmeas.2021.106626

61. Braby LA. Ionization in microscopic volumes irradiated by energetic photons. In: *Radiological physics*. Oregon State University (1972).

62. Magrin G, Barna S, Meouchi C, Rosenfeld A, Palmans H. Energy-loss straggling and delta-ray escape in solid-state microdosimeters used in ion-beam therapy. *J Nucl Eng* (2022) 3(2):128–51. doi:10.3390/jne3020008

63. Fattori S, Petringa G, Agosteo S, Bortot D, Conte V, Cuttone G, et al. (4)He dose- and track-averaged linear energy transfer: Monte Carlo algorithms and experimental verification. *Phys Med Biol* (2022) 67(16). doi:10.1088/1361-6560/ac776f

64. Parisi G, Bianchi L, Couture P, Palitsin V, Fabbri A, Schettino G, et al. The border effect in diamond microdosimeters and its impact on hadron therapy applications. *Phys Med and Biol* (2025) 70(3):035003. doi:10.1088/1361-6560/adaace

65. Bolst D, Guatelli S, Tran LT, Chartier L, Davis J, Biasi G, et al. Validation of Geant4 for silicon microdosimetry in heavy ion therapy. *Phys Med and Biol* (2020) 65(4):045014. doi:10.1088/1361-6560/ab586a

66. Gehrke T, Burigo L, Arico G, Berke S, Jakubek J, Turecek D, et al. Energy deposition measurements of single 1 H, 4 He and 12 C ions of therapeutic energies in a silicon pixel detector. *J Instrumentation* (2017) 12:P04025. doi:10.1088/1748-0221/12/04/p04025

67. Arico G, Gehrke T, Jakubek J, Gallas R, Berke S, Jäkel O, et al. Investigation of mixed ion fields in the forward direction for 220.5 MeV/u helium ion beams: comparison between water and PMMA targets. *Phys Med Biol* (2017) 62(20):8003–24. doi:10.1088/1361-6560/aa875e

68. Gallas RR, Arico G, Burigo LN, Gehrke T, Jakůbek J, Granja C, et al. A novel method for assessment of fragmentation and beam-material interactions in helium ion radiotherapy with a miniaturized setup. *Phys Med* (2017) 42:116–26. doi:10.1016/j.ejmp.2017.09.126

69. Meouchi C. Microdosimetry of a clinical carbon-ion pencil beam at MedAustron - part 1: experimental characterization. *Z Med Phys* (2025). doi:10.1016/j.zemedi.2025.06.003

70. Guatelli S, Reinhard MI, Mascialino B, Prokopovich DA, Dzurak AS, Zaider M, et al. Tissue equivalence correction in silicon microdosimetry for protons characteristic of the LEO space environment. *Nucl Sci* (2009) 55:3407–13. doi:10.1109/tns.2008.2006894

71. Bolst D, Guatelli S, Tran LT, Chartier L, Lerch MLF, Matsufuji N, et al. Correction factors to convert microdosimetry measurements in silicon to tissue in (12)C ion therapy. *Phys Med Biol* (2017) 62(6):2055–69. doi:10.1088/1361-6560/aa5de5

72. Stasica P, Nguyen H, Granja C, Kopeć R, Marek L, Oancea C, et al. Single proton LET characterization with the Timepix detector and artificial intelligence for advanced proton therapy treatment planning. *Phys Med Biol* (2023) 68(10). doi:10.1088/1361-6560/acc9f8

73. Hoang S, Vilalta R, Pinsky L, Kroupa M, Stoffle N, Idarraga J. Data analysis of tracks of heavy ion particles in timepix detector. *J Phys Conf Ser* (2014) 523(1):012026. doi:10.1088/1742-6596/523/1/012026

74. Cordoni FG, Missiaggia M, Scifoni E, La Tessa C. Cell survival computation via the generalized stochastic microdosimetric model (GSM2); part I: the theoretical framework. *Radiat Res* (2021) 197(3):218–32. doi:10.1667/RADE-21-00098.1

75. Sato T, Furusawa Y. Cell survival fraction estimation based on the probability densities of domain and cell nucleus specific energies using improved microdosimetric kinetic models. *Radiat Res* (2012) 178(4):341–56. doi:10.1667/rr2842.1

76. Hartzell S, Furutani KM, Parisi A, Sato T, Kase Y, Deglow C, et al. Impact of microdosimetric modeling on computation of relative biological effectiveness for carbon ion radiotherapy. *Radiation* (2025) 5(2):21. doi:10.3390/radiation5020021

77. Wong WS, Alozy J, Ballabriga R, Campbell M, Kremastiotis I, Llopart X, et al. Introducing Timepix2, a frame-based pixel detector readout ASIC measuring energy deposition and arrival time. *Radiat Measurements* (2020) 131:106230. doi:10.1016/j.radmeas.2019.106230

78. Llopart XA, Ballabriga R, Campbell M, Casanova R, Gromov V, Heijne EHM, et al. *Timepix4, a large area pixel detector readout chip which can be tiled on 4 sides providing sub-200 ps timestamp binning. 22nd international workshop on radiation imaging detectors* (2021).

79. Oancea C High-count-rate particle tracking in proton and carbon radiotherapy with Timepix2 operated in ultra-short acquisition time. (2024).

80. Novak A, Granja C, Sagatova A, Jakubek J, Zatko B, Vondracek V, et al. Silicon Carbide Timepix3 detector for quantum-imaging detection and spectral tracking of charged particles in wide range of energy and field-of-view. *J Instrumentation* (2023) 18(11):C11004. doi:10.1088/1748-0221/18/11/c11004